



Radio Science®

RESEARCH ARTICLE

10.1029/2021RS007338

Key Points:

- Physics-based seasonal-daily noise level model built for pole-oriented high-frequency radars
- Good agreement between modeled noise level and experimental observations
- Model allows estimating vertical absorption from noise measurements at these radars

Supporting Information:

Supporting Information may be found in the online version of this article.

Correspondence to:

J.-P. St- Maurice, jp.stmaurice@usask.ca

Citation:

Berngardt, O. I., St- Maurice, J.-P., Ruohoniemi, J. M., & Marchaudon, A. (2022). Seasonal and diurnal dynamics of radio noise for 8–20 MHz poleward-oriented mid-latitude radars. *Radio Science*, 57, e2021RS007338. https://doi.org/10.1029/2021RS007338

Received 24 JUL 2021 Accepted 27 AUG 2022

Seasonal and Diurnal Dynamics of Radio Noise for 8–20 MHz Poleward-Oriented Mid-Latitude Radars

O. I. Berngardt¹, J.-P. St- Maurice², J. M. Ruohoniemi³, and A. Marchaudon⁴

¹Institute of Solar-Terrestrial Physics, SB RAS, Irkutsk, Russia, ²Institute of Space and Atmospheric Studies, University of Saskatchewan, 116 Science Place, Saskatoon, SK S7N 5E2, Canada, ³Bradley Department of Electrical and Computer Engineering, Virginia Polytechnic Institute and State University, Blacksburg, VA, USA, ⁴Research Institute in Astrophysics and Planetology (IRAP), Toulouse University, CNRS, CNES, Toulouse, France

Abstract Based on ray tracing in a smooth ionosphere described by the IRI-2012 model we have inferred the seasonal-diurnal dynamics of radio noise observed by four mid-latitude high-frequency (HF) radars. In the calculations, noise is assumed to be homogeneous and stationary, but the main contribution comes from the radar skip zone boundary due to focusing radiowaves effect. Noise absorption along the ray path is simulated from the IRI-2012 electron density, and from the molecular nitrogen density and electron temperatures obtained from the NRLMSISE-00 model. Earth magnetic field is not taken into account both in the absorption and ray-tracing calculations due to insufficient accuracy of the ionospheric model. The model results are compared with experimental radar data, and good agreement between the two is demonstrated. It is shown that experimentally observed seasonal and diurnal dynamics of the noise correlates well with model predictions. We demonstrated saturation effect at low noise levels. The model makes it possible to estimate the amount of absorption in D- and E-layers using noise observations at SuperDARN and SuperDARN-like poleward-oriented radars, especially at mid-latitudes. This is important for the retrieval of long term variations in the electron density in the lower ionosphere, by using wide coverage provided by these radars' network. The model also makes it feasible to interpret vertical absorption by experimental noise observations, thereby significantly expanding the capability of HF radars to monitor the lower ionosphere, and to provide data for joint analysis with other data, obtained by these radars at E- and F-layer heights.

1. Introduction

Noise level studies have recently become an integral part of theoretical and applied research on lower ionosphere dynamics during solar flares and coronal mass ejections through the use of SuperDARN and similar high-frequency (HF) radars (Berngardt, 2020; Berngardt et al., 2018, 2019; Bland et al., 2018, 2019). HF noise has traditionally been considered to come from a mixture of several components—anthropogenic, cosmic, and atmospheric.

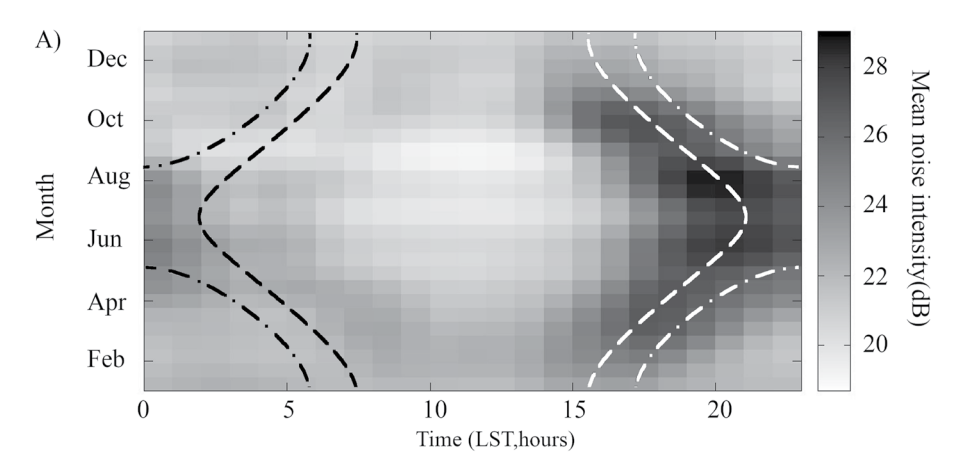
For radars with an equatorward field of view, it has been assumed that the main contribution to observed HF noise originates from tropical lightning discharges and that the signals from these discharges propagate over large distances through the ionospheric waveguide (Pederick & Cervera, 2014). Modeling based on this notion has been validated reasonably well, with noise levels predictions close to experimental observations.

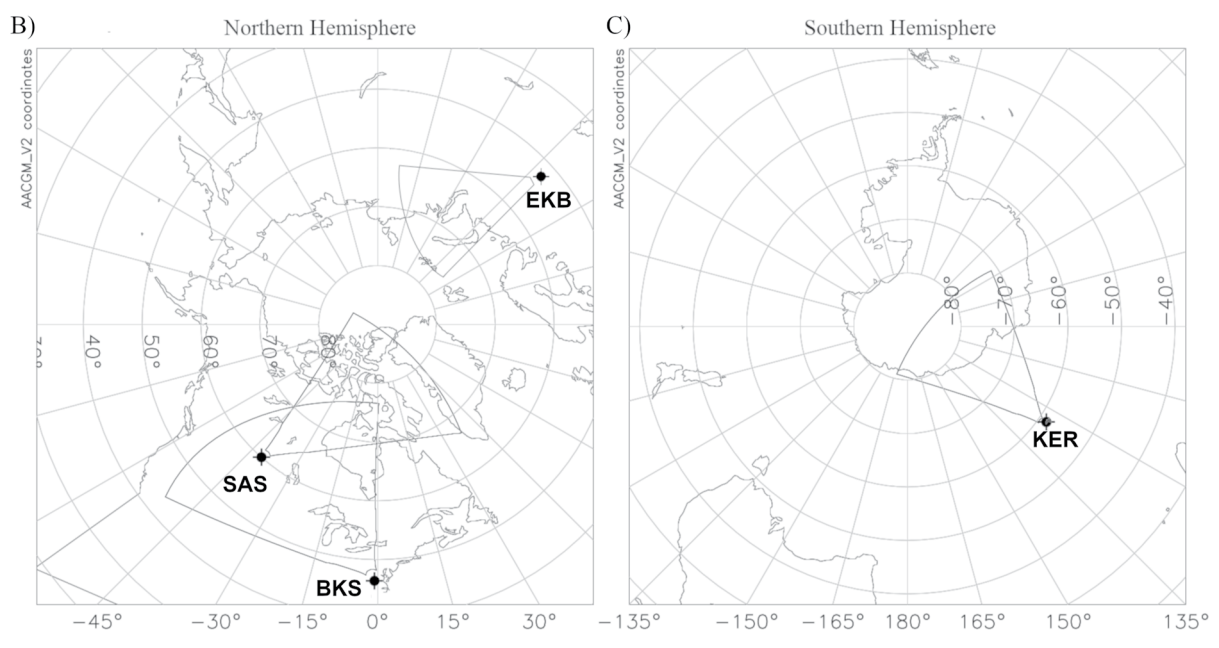
In studies by Ponomarenko et al. (2016) and Berngardt (2020), seasonal-diurnal variations of the minimum noise level were measured by the mid-latitude SAS and EKB radars at a fixed frequency. In this paper we refer to radars, including SAS, as mid-latitude radars for having geographic latitudes lower than 60°. The fields of view of both radars point toward the polar regions and the shapes of the seasonal-diurnal dependence as a function of local solar time are similar. As illustrated in (Figure 1a), they take the form of an oval, the contour of which is determined by the position of the solar terminator. This stated, there is no obvious reason why the HF noise observed in mid-latitude poleward pointing radars like SAS and EKB should be closely associated with lightning. In addition, the ray paths emerging from equatorial sources are so long that the noise should be absorbed almost completely for daytime conditions. For night time conditions, this may not be obvious owing to a lack of absorption on the way to the antenna backlobe. We have ran simulations (not shown) for the EKB radar for which the antenna beam pattern was known quite precisely and found that the signal would remain 10–20 dB stronger in the front lobe even at night. The only exception was for morning conditions. However, the total attenuation due to absorption in that case was so large that the fact that the back lobe had less absorption did not matter.

© 2022. American Geophysical Union. All Rights Reserved.

BERNGARDT ET AL. 1 of 20

1944799s, 2022, 9, Downbaded from https://agupubs-onlinelibrary.wiley.com/doi/10.1029/021R8007338 by Virginia Tech, Wiley Online Library on [12/05/2023]. See the Terms and Conditions (https://onlinelibrary.wiley.com/terms-and-conditions) on Wiley Online Library for rules of use; OA articles are governed by the applicable Creative and Conditions (https://onlinelibrary.wiley.com/terms-and-conditions) on Wiley Online Library for rules of use; OA articles are governed by the applicable Creative and Conditions (https://onlinelibrary.wiley.com/terms-and-conditions) on Wiley Online Library for rules of use; OA articles are governed by the applicable Creative and Conditions (https://onlinelibrary.wiley.com/terms-and-conditions) on Wiley Online Library for rules of use; OA articles are governed by the applicable Creative and Conditions (https://onlinelibrary.wiley.com/terms-and-conditions) on Wiley Online Library for rules of use; OA articles are governed by the applicable Creative and Conditions (https://onlinelibrary.wiley.com/terms-and-conditions) on Wiley Online Library for rules of use; OA articles are governed by the applicable Creative and Conditions (https://onlinelibrary.wiley.com/terms-and-conditions) on Wiley Online Library for rules of use; OA articles are governed by the applicable Creative and the applicable Creative an





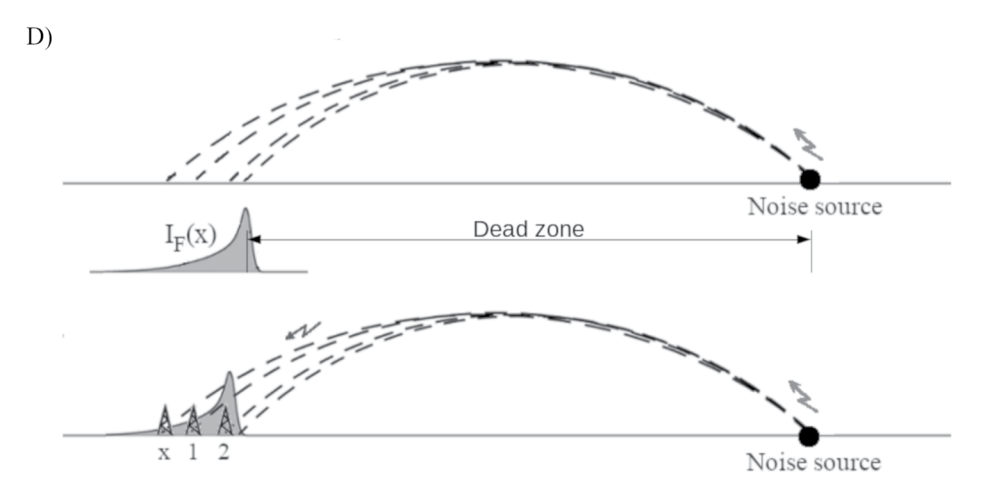


Figure 1.

BERNGARDT ET AL. 2 of 20

1944799x, 2022, 9, Downloaded

com/doi/10.1029/2021RS007338 by Virginia Tech, Wiley Online Library on [12/05/2023]. See

are governed by the applicable Creative Commons Licens

Mathematical empirical approaches have been introduced to reproduce noise patterns of the kind shown in Figure 1a, irrespective of the physical origin of the patterns. One such approach uses the mean daily dynamics of noise level over the previous 30 days (Bland et al., 2018). Another consists of using special auto-regressive models (Berngardt, 2020). While these models have their usefulness, no physical model has apparently been built to this day to reproduce the seasonal-daily dependence of the noise pattern for poleward-oriented radars. In this paper, we build an approach close to the approach used for interpretation of the noise at equatorward-oriented radars by Pederick and Cervera (2014, 2016), but built in the absence of strong thunderstorm centers, based on focusing effect of the homogeneous ground noise only, more adequate to the observations at poleward-oriented radars. One clear advantage of building such a physical model would be the ability to predict a "quiet-day" curve at poleward-oriented radars, namely, a curve of the expected noise level for ordinary ionospheric conditions. Reproducing an observed quiet-day curve would make it possible to estimate the vertical absorption level, allowing for the extraction of the long-period variations associated with the D- and E-layers of the ionosphere. In turn, building a physical model of noise level would make it feasible to effectively use SuperDARN and similar radars for estimating the electron density in the lower part of the ionosphere.

With the above in mind, we have developed a physics-based numerical model of the noise at HF frequencies. We have applied the results of the model to the seasonal-diurnal dynamics of noise level at four mid-latitude radars, namely, the Canadian SAS SuperDARN radar (52.2°N and 106.5°W), the US BKS SuperDARN radar (37.1°N and 78.0°W), the French KER SuperDARN radar (Southern French Territory, 49.2°S and 70.1°E), and the Russian EKB ISTP SB RAS radar (56.5°N and 58.5°E). Each of these radars has a field of view with an antenna beam pattern that points nearly poleward (Figures 1b and 1c), having front-to-back lobe ratios of at least 10 dB meaning that the influence of tropical thunderstorm centers on the noise production should be negligible. We describe our model in Section 2. In Section 3, we present its results and compare with observations while discussing the implications for the plasma densities in the lower ionosphere. Our conclusions are presented in Section 4.

2. Description of the Physics-Based Noise Model

Our model is based on a mechanism proposed by Berngardt et al. (2018, 2019). It assumes that the noise level in polar-oriented radars operating in the 8-20 MHz range is determined by a focusing of noise signals from various anthropogenic sources, and that the main sources contributing to the noise are located around the boundary of the so-called "skip zone." Near the skip zone, the amplitude of propagating signals is amplified significantly due to spatial focusing of radiowaves by the ionosphere (Tinin et al., 1992).

Figure 1. (a) Seasonal-diurnal pattern of average noise intensity at the EKB radar (Berngardt, 2020). The lines correspond to the position of solar terminator at two different heights (at ground level—dashed line and at 300 km height—dot-dashed line); (b and c) fields of view, in AACGMv2 (Shepherd, 2014) geomagnetic coordinates, of the four mid-latitude radars involved in the current study, for the Northern and Southern hemispheres; and (d) noise propagation and collecting scheme for the proposed model, illustrating the focusing mechanism for enhancing the intensity, $I_F(x)$, around the boundary of the skip zone (equivalently labeled as the "dead zone" in the cartoon).

BERNGARDT ET AL. 3 of 20

om/doi/10.1029/2021RS007338 by Virginia Tech, Wiley Online Library on [12/05/2023]. See

Within the framework of this model, the following factors need to be considered:

- 1. the spatial distribution of the amplitudes of the sources of noise and the noise emission direction pattern for each source;
- 2. the ray path of the radio signals in an irregular ionosphere;
- 3. the intensity produced by the focusing of radio signals on the boundary of the skip zone;
- 4. the absorption of the signal over the ray path as it passes through the D- and E-regions; and
- 5. the antenna beam pattern of the radar receiver.

In general, each of the above characteristics has its own temporal and frequency dependencies. This stated, in the following calculations, we assumed that noise sources approximately have an isotropic directional pattern, equal amplitudes, and are uniformly distributed over the Earth's surface around the radar. In the presence of intense localized anthropogenic sources (radio stations, industrial sources, railways) or for radars facing thunderstorm activity centers, this assumption has to obviously break down. However, for radars located at a significant distance from intense anthropogenic or thunderstorm activity centers, this assumption should be reasonable for an initial study of the kind offered in that present paper. The ultimate test of the validity of our assumption will, clearly, rest on a comparison of the theoretical predictions against observations. We expect that individual point sources, while real, will only make minor contributions to the minimal noise level, measured by a radar, in general.

To be specific, according to the interpretation suggested by Berngardt et al. (2018, 2019) and Berngardt (2020) noise propagates from a noise source and focuses just beyond the boundary of the source's skip zone, as illustrated in Figure 1d. Within that framework the noise received by a radar is a superposition (integral) of noise source contributions with weights defined by skip zone multiplier I_F calculated for the radar position. The integration is made over the azimuth θ , elevation α , and range s. It takes into account the antenna beam pattern, signal attenuation with distance and signal attenuation due to absorption in the lower ionosphere. This means that, to a first approximation, the noise intensity received by the radar, I_{rev} , can be obtained from the expression

$$I_{rcv} \approx \int_{\Omega, S} I_{src} \left[x(\alpha, \theta) \right] I_F \left[x(\alpha, \theta, s) - x_0(\alpha, \theta) \right] A_t(\alpha, \theta) G(\alpha, \theta) s^{-2} \cos(\alpha) d\alpha d\theta ds \tag{1}$$

where I_{src} is the noise intensity distribution of the noise source at the ground, I_F is the skip zone focusing multiplier, s is the distance from the source to the receiver, and s^{-2} is the attenuation in intensity due to distance. Also, $G(\alpha, \theta)$ is the shape of the antenna beam pattern, and $A_t(\alpha, \theta)$ is the absorption over the trajectory of a ray. In these expressions s is a phase path length along a ray that starts at specific values of s and s, whereas s is the phase path length at the focusing point, namely, at the skip zone boundary. It should be understood that s does not depend on s but that s does depend on s because the integration is over the distances of the various noise sources to the receiver. In other words, the s and s integrations are over the receiver angles, while the integration over s is actually over the distance of the noise sources to the radar.

As a further approximation, we assume that the variations of the various parameters are such that the noise intensity I_{rev} can be described accurately enough with the simpler expression

$$I_{rcv} \approx I_0 \overline{I_F} A_t G_A \overline{A_R}$$
 (2)

where I_0 is the intensity of ground noise sources and replaces the I_{src} if the latter can be assumed to be isotropic (later in our simulations I_0 is used as a normalization constant, calculated over 1 year). For further analysis we will use only relative power I_{rcv} in dB, normalized to yearly maximum. After normalization the I_0 constant will be excluded, same as all other multiplicative constants, such as antenna gain or receivers amplification, that are not shown in this formula. Therefore, the constant I_0 will not affect the seasonal-daily dynamics of the noise level and can be neglected in the forth coming analysis made in the paper. Its absolute value relates with the intensity of the background noise, receivers attenuation, and all other possible factors, considered to be nearly constant over the year. The term $\overline{I_F}$ is the integral over all distances to the source of the focusing intensity at the boundary of the skip zone, whereas A_t becomes the absorption of the radio signal power over the whole ray path, and G_A is the beam pattern of the receiving antenna integrated over θ , that is, over all azimuths. Also, $\overline{A_R}$ is the integrated signal attenuation with respect to distance. Consistent with this definition, the \overline{a} symbol describes an averaging of quantity a over the range. This means that to

BERNGARDT ET AL. 4 of 20

.1029/2021RS007338 by Virginia Tech, Wiley Online Library on [12/05/2023]. See the Terms

obtain Equation 2 we replaced the average value of the product of the various non-negative parameters in Equation 1 by the product of the average values of the parameters with a single ray path from the border of the radar skip zone.

Finally, taking into account that power attenuates with propagation trajectory length s as s^{-2} , we can estimate:

$$\overline{A_R} \approx \int_S^{S_{\text{max}}} s^{-2} ds \approx S^{-1}$$
 (3)

This result is valid as long as $S \ll S_{\text{max}}$ (maximal radar range).

At a fixed frequency, we can assume I_0 to be constant. This holds if we can assume to first order that the various noise sources are not only isotropic, but also homogeneous, incoherent, and equal in intensity. This is a rather rough assumption, but, as shown below, it proves to be sufficient for an adequate modeling of the noise pattern.

2.1. The Propagation Trajectory

Propagation trajectories were obtained with the use of wave optics based on a calculation made at fixed pre-determined starting values of the elevation angles within 0° – 90° with 0.09° steps. For a given azimuthal direction or radar beam we could describe the system in terms of spherical coordinates for the radial distance ρ and the elevation angle ϕ . We restricted the calculations to the HF limit for the index of refraction, n, and did not include absorption in the calculations, that is, we used the ordinary wave expression given by

$$n^2 = 1 - f_e^2 / f_0^2 \tag{4}$$

where f_e and f_0 are the plasma frequency and radar frequency, respectively. For this situation the differential equations leading to phase and group delays as a function of starting elevation angles can be described by the following set of equations (Kraytsov & Orlov, 1983):

$$\begin{cases} \frac{\partial R_{\rho}}{\partial S} = P_{\rho} \\ \frac{\partial R_{\phi}}{\partial S} = \frac{1}{R_{\rho}} P_{\phi} \\ \frac{\partial P_{\rho}}{\partial S} = \frac{f_{e}}{f_{0}^{2}} \frac{\partial f_{e}}{\partial R_{\rho}} + \frac{1}{R_{\rho}} P_{\phi}^{2} \\ \frac{\partial P_{\phi}}{\partial S} = \frac{1}{R_{\rho}} \left(\frac{f_{e}}{f_{0}^{2}} \frac{\partial f_{e}}{\partial \phi} - P_{\rho} P_{\phi} \right) \\ \psi = \psi_{0} + \int_{S_{0}} P^{2} dS \end{cases}$$

$$(5)$$

where \overline{R} is the radius vector describing the position of the wave impulse at a particular point in the trajectory and where \overline{P} is the wave impulse, while ψ is the phase path (or eikonal). Integration was carried over the trajectory variable s with starting and end points at S_0 and S, and with ψ_0 being associated with the initial value of the eikonal. In such calculations, the regions where phase delay goes through an extremum (minimum) correspond to the regions of focusing, that is to say, they describe the borders of the skip zone for different propagation modes.

In model numerical calculations we assumed that the radio waves propagated in a plane made of a given azimuth in one direction and a number of elevations angles that followed a globe arc within a spherical Earth model. This stated, our ionospheric model remained inhomogeneous in the propagation plane, as it depended on the distance to the source and on elevation angle. In other words, the ionospheric propagation model remained a function of latitude and altitude. Specifically, we used the IRI-2012 (Bilitza et al., 2014) ionospheric model for our purpose. This model is not a recent one, but it corresponds well to the time period of interest to our modeling (the year 2013). Note that, except for the D-region, we used the default options posted in https://irimodel.org/IRI-2012/00_iri2012_readme.txt. As described below in some detail, for the *D* region, we explored three different options.

BERNGARDT ET AL. 5 of 20

It has become apparent in more recent years that IRI can produce significant errors at high latitudes (Bjoland et al., 2016; Themens et al., 2014). Other models exist, that are reported to be more accurate especially in those regions (Shubin, 2017; Themens, Jayachandran, McCaffrey, Reid, et al., 2019; Themens et al., 2017). Nevertheless, having focused for the statistical study on regular, mostly quiet geomagnetic conditions, we have deemed that the IRI model remained quite adequate. Indeed, IRI has frequently been a standard model for all the radars of interest to the present study, this for all directions of interest (beams), whether the look direction was poleward or off-poleward. Taking into account both the high-latitude and the mid-latitude ionosphere in both hemispheres, this has proven to be very important for the ray-tracing task.

Finally, we also note that, in order to work with a smooth and continuous ionosphere along ray trajectories, it was necessary to assume that the signal propagation plane did not depend on the starting elevation angle when seeking numerical solutions to the set of differential Equation 5. While correct for the middle(central) beams of the radar antenna pattern, this was not strictly true for the extreme ones, since the antenna beam pattern is actually described by a conical shape (Shepherd, 2017). But, as will be shown later, this rough approximation is sufficient for carrying the model calculations forward with reasonable accuracy.

For the specific ray path calculations we used a grid with step sizes of 222 km (equivalent to 2° in latitude at Earth's surface) in distance and 3 km in height in the propagation plane. For calculations between grid points, an interpolation was performed using two-dimensional local quadratic B-splines to obtain continuous values and smooth spatial derivatives. When later adding absorption effects we used the NRLMSISE-00 model for the neutral atmosphere, from which we extracted the molecular nitrogen density and the electron temperature interpolated between grid points in the same way.

2.2. Modeling the Focusing Near the Skip Zone Boundary

2.2.1. Determining $\overline{I_F}$

In a two-dimensional situation such as the one used here, the focusing of the radio waves emitted from a point source can be described analytically near the skip zone, if the ionospheric peak can be approximated by a parabola. In that case, if we neglect insignificant multipliers, the signal amplitude $A_F(x)$ over the phase path length x has a well-known dependence given by (Tinin et al., 1992):

$$A_F(x) \sim \frac{1}{\Lambda} Ai \left(\frac{2^{2/3}}{\Lambda} \left[\overline{x} - x \right] \right)$$
 (6)

1029/2021RS007338 by Virginia Tech, Wiley Online Library on [12/05/2023]. See

where Ai() is the Airy function describing the shape of the signal focusing versus phase path length, and where

$$\Lambda = \left(\frac{1}{2k^2} \frac{\partial^2 \overline{x}}{\partial \alpha^2}\right)^{1/3} \tag{7}$$

is a quantity inversely proportional to the size of the focusing area associated with the second derivative of the phase path length over the elevation angle α . Here, k is wavenumber. Note that Equation 6 does not take into account the decay of the wave field with distance and strong horizontal spatial gradients of electron density.

By integrating Equation 6 over the range, and taking into account that noise sources are independent, it therefore follows that the range-integrated power $\overline{I_F}$, corresponding to the total power of the noise superposed from various noise sources homogeneously placed at different ranges is given, to a first approximation, by:

$$\overline{I_F} \sim \frac{1}{\Lambda} \int Ai^2 \left(\overline{\eta} - \eta \right) d\eta \tag{8}$$

where the integration is made over the dimensionless quantity $\eta = 2^{2/3}x/\Lambda$ and $\overline{\eta} \gg 1$.

This means that the focusing power $\overline{I_F}$ in Equation 2 thus can be approximated reasonably well with the simple expression:

$$\overline{I_F} \sim \frac{1}{\Lambda}$$
 (9)

BERNGARDT ET AL. 6 of 20

2.2.2. Determination of the Skip-Zone Position

To find the propagation path of the focusing signal in an arbitrary ionosphere, it is necessary in the context of wave optics to extract the dependence of the phase delay ψ on the elevation angle α . We use the fact that, at the focal points, the phase delay dependence on the elevation angle is weakest, meaning that the derivative of the phase becomes zero (Tinin et al., 1992). Since we considered many possible ray paths, the focal points spread into a small area. Qualitatively, the size of such an area is a measure of the number of rays arriving at the receiving point with the same phase, thereby adding to the total amplitude of the received noise signal through constructive interference of the rays. In terms of our model, this size is inversely proportional to the cubic root of the second derivative of the phase delay over the elevation angle (Equation 7) at the point where the first derivative becomes zero (i.e., near the skip zone border), so that the power of the focused signal is proportional to the size of this area (Kravtsov, 1968).

It is obvious that in a complex ionosphere there can be several focusing regions (modes). To find the positions (elevation angles) of the groundscatter modes, we analyzed all the possible propagation trajectories by calculating the phase delay ψ for each elevation angle α_i . After calculating the dependence of the phase delay on the elevation angle $\psi(\alpha)$ the elevation angles α_i of the rays getting to the skip zones were determined from the position where the phase delay reached its minimal value:

$$\alpha_i : \left. \frac{d\psi(\alpha)}{d\alpha} \right|_{\alpha = \alpha} = 0 \tag{10}$$

.1029/2021RS007338 by Virginia Tech, Wiley Online Library on [12/05/2023]. See

We should add that the local dependence $\psi(\alpha)$ was fitted to a parabola to make the evaluation of the second derivative of $\psi(\alpha)$ easier for the determination of Λ (Equation 7).

We obtained a collection of angles α_i corresponding to different groundscatter modes. In a regular, spherically layered, non-magnetized, parabolic ionosphere, there is usually no more than one ground-scatter mode—there is only one local minimum of the phase-elevation characteristic. In a more complex but more realistic heterogeneous multi-layer ionosphere, there can be several groundscatter modes, with the presence of a magnetic field possibly adding extra possibilities. Just with the propagation of ordinary rays, we found many instances of multiple ground-scatter modes, each with its own phase, group delay and central elevation angle α .

Examples of electron density profiles at different local times, as well as phase and group delay for single-mode (black line) and multi-mode (red and green lines) signals, calculated using the IRI-2012 model, are shown in Figures 2a–2c. Modeling was carried out for the EKB radar (56.5°N, 58.5°E), for the northern direction of radio wave propagation (azimuth 0, beam 2), for 1 June 2013. It can be seen from the figure that several modes correspond to several well-defined (E and F) layers in the electron density.

When multi-mode noise trajectories were obtained, we chose the mode (trajectory) that contributed the most to the noise signal intensity, after having taken signal absorption and antenna pattern attenuation into account. Following this, the modeled noise level was chosen to be the intensity of the mode with maximum intensity after taking all factors into account, namely, propagation, absorption, and antenna beam pattern.

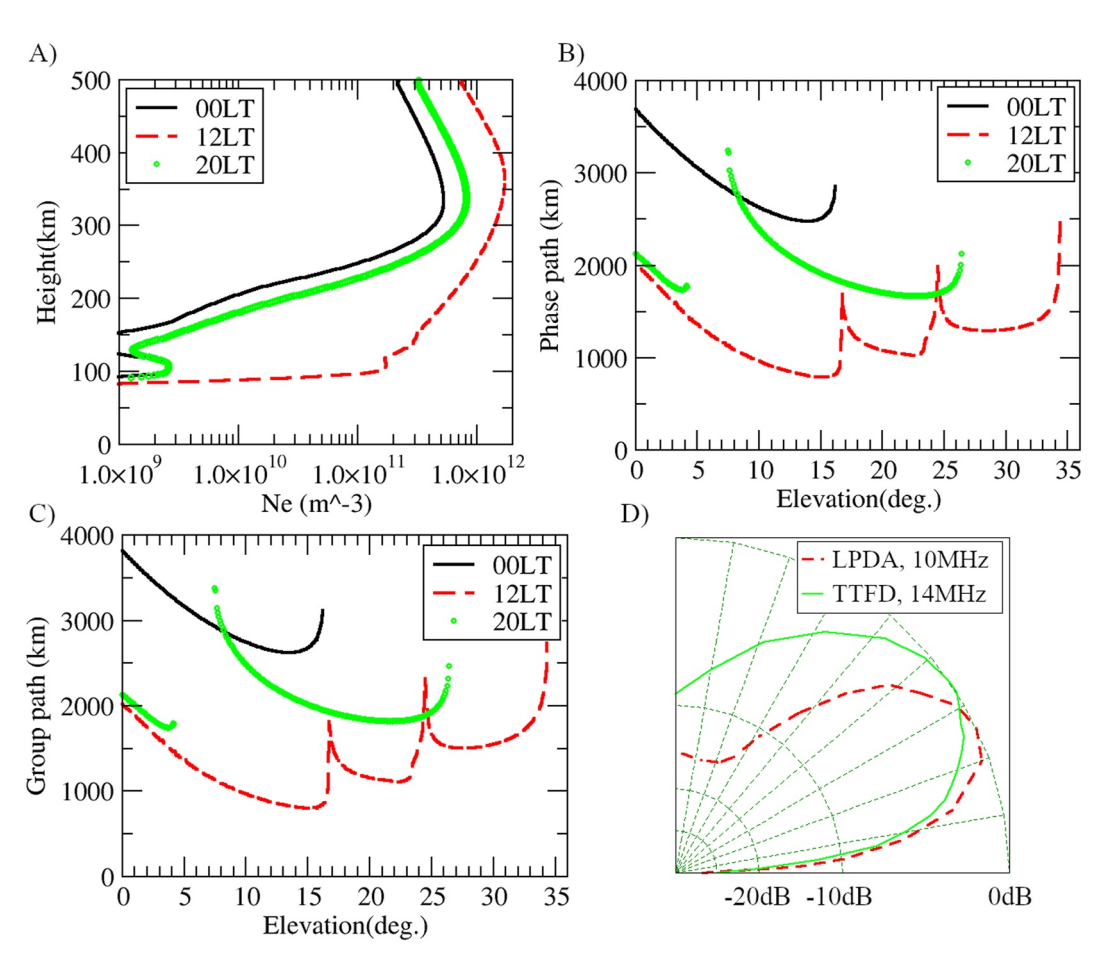
2.3. Antenna Pattern

Another important parameter of the model is the signal attenuation due to the antenna pattern G_A . The attenuation can reach several tens of dB, and therefore it is very important to take it into account at low and high elevation angles. In this paper, we have dealt with the data from several radars: EKB from ISTP SB RAS, and SAS, KER, and BKS from SuperDARN. Every one of these radars has a different type of antenna and a different G_A .

Taking into account that the azimuthal width of the antenna beam pattern is defined by a phased array geometry and size considerations (that much is similar for all the radars under consideration), the integrated antenna multiplier G_A has been taken to simply be proportional to the antenna pattern in the elevation plane, that is to say:

$$G_A(\alpha) = \int_{\Omega} G(\alpha, \Theta) d\Theta \approx G(\alpha) \Delta\Theta \tag{11}$$

BERNGARDT ET AL. 7 of 20



1944799x, 2022. 9, Downloaded from https://agupubs.onlinelibrary.wiley.com/doi/10.1029/2021RS007338 by Virginia Tech, Wiley Online Library on [12/05/2023]. See the Terms and Conditions (https://onlinelibrary.wiley.

Figure 2. (a–c) Examples of electron density profile (a), phase path (b), and group path (c), calculated using the IRI-2012 model for the EKB radar for the north-facing direction on 1 June 2013; (d) model radar antenna beam patterns in the elevation plane used in our various simulations: Log-Periodic Dipole Array (LPDA) beam model at 10 MHz for the EKB, SAS, and KER radars (Arnold et al., 2003; Berngardt et al., 2020), and Twin Terminated Folded Dipole (TTFD) beam model at 14 MHz for the BKS radar (Sterne et al., 2011).

where $\Delta\Theta$ is the azimuthal beam width of the phased array antenna beam pattern and is the same for all the radars considered here. In addition, $G(\alpha)$ is the antenna beam pattern of a single antenna in the elevation plane.

Figure 2d shows the model antenna beam patterns of the various radars at 10–14 MHz frequency that were used for our modeling. It should be noted that the main difference between the various antenna beam patterns comes from the fact that the EKB, SAS, and KER radars use Log-Periodic Dipole Array antennas at the top of masts approximately 15 m above the ground (Arnold et al., 2003; Berngardt et al., 2020), while the BKS radar uses Twin Terminated Folded Dipole antennas at a lower height (Sterne et al., 2011). This significantly increases the amplitude of the vertical lobe on the BKS radar and broadens its elevation antenna pattern as compared to the EKB, SAS, and KER radars.

2.4. Noise Absorption Over the Trajectory

Another important parameter affecting the radio noise intensity is the absorption of the signal over the propagation trajectory. The absorption per unit length L[dB] was calculated within the framework of a classical model by Zawdie et al. (2017) in which frequencies are considered to be high enough to justify neglecting magnetic field effects:

$$L[dB] = -\frac{20}{\log(10)} \frac{e^2}{2\epsilon_0 m_e c} \frac{n_e \nu_e}{\nu_e^2 + (2\pi f_0)^2}$$
(12)

BERNGARDT ET AL. 8 of 20



where, as before, f_0 is the operating frequency of the radar, n_e is the electron density, and m_e , c, e_0 are the electron mass, the speed of light in vacuum and the dielectric constant of vacuum, respectively, while ν_e is the effective electron collision frequency. Since ν_e is only effectual in the lower part of the ionosphere we considered it to be equal to the electron collision frequency with molecular nitrogen ν_{e,N_2} . Following Schunk and Nagy (2000), it was assumed to be given by

$$v_e \simeq v_{e,N_2} = 2.33 \cdot 10^{-11} \cdot n_{N_2} \left(1 - 1.21 \cdot 10^{-4} T_e \right) T_e$$
 (13)

where n_{N_2} is the molecular nitrogen density and T_e is the electron temperature. The accuracy of this approximation has been discussed in detail by Zawdie et al. (2017).

The total absorption of the radio wave $L_{int}[dB]$ was calculated as the integral of the unit absorption over the propagation trajectory S, namely (Zawdie et al., 2017):

$$L_{int}[dB] = \int_{S} L[dB]ds \tag{14}$$

In the simulations, the absorption was taken into account only for the D- and E-layers, namely, in the 60–120 km altitude range, where significant contributions to the absorption were possible if n_e was potentially large enough and where the collision frequency could compete with f_0 . For our model simulations, we describe the absorption factor A_e , in Equation 2 with

$$A_t = \exp\left(\frac{\ln(10)}{10}L_{int}[dB]\right) \tag{15}$$

2.4.1. Weighting the Factors That Control the Absorption

To evaluate the absorption of the radio signal from the above expression, we used well-known empirical models, namely, the IRI-2012 model for a determination of the electron density n_e , and the NRLMSISE-00 model for a determination of the effective electron collision frequency based on the density of molecular nitrogen n_{N_2} and the electron temperature T_e . As already mentioned at the end of section 2.1, in the plane of the propagation trajectory of the radio signal, the absorption was tabulated over a grid which had 222 km range resolution and 5 km height resolution. For calculations between grid points, interpolation was performed with two-dimensional local quadratic B-splines to obtain continuous values required for trajectory calculations.

One source of uncertainty in the absorption calculation comes from accounting for the electron density in the D-layer, which is no easy task, to say the least (Bilitza & Reinisch, 2008; Danilov et al., 2002). Even the standard Reference ionospheric model, IRI-2012, includes several different models for electron density at heights 65–110 km. To demonstrate the complicated task at hand, Figure 3a shows a comparison of the monthly average level of electron density at 75 km height between three electron density models for March 2013. While we used the standard IRI-Ne D-layer model incorporated in the older IRI-95 model (Bilitza, 1981, 1997), two other models were also inserted in its place into the IRI-2012 calculations: the FIRI Faraday-International Reference Ionosphere (Friedrich & Torkar, 2001) and Danilov's model (Danilov et al., 1995). All three D-region models were obtained from the OUTF(14,*) array from the IRI code.

Figure 3a shows that there are clearly important differences in the *D* region between the models. In particular, the nighttime electron density level could be significant (as demonstrated, e.g., in Gomonov et al. (2019)) and should be taken into account when simulating the diurnal variation of the absorption. Taking this into account leads us to conclude that the diurnal variation of the absorption inferred from the radar measurements is associated not with the absolute value of the electron density, but with its variation over its minimum (nighttime) value. This means that the absolute electron density of the D-layer cannot be correctly determined through coherent scatter radar absorption data using noise level observations without a very careful analysis of the latter and without an absolute calibration of these observations on a long term basis. A comparison between observations and numerical prediction is done in the next subsection.

Before a detailed comparison we want to illustrate the effect of seasonal variations on absorption, Figures 3b and 3c show plots of the unit absorption per kilometer of the trajectory L[dB] as a function of altitude that were calculated for May and November of 2013 to the North of the EKB radar (azimuth 0°, radar beam 2), using

BERNGARDT ET AL. 9 of 20

1944799x, 2022. 9, Downloaded from https://agupubs.onlinelibary.wiley.com/doi/10.1029/2021R8007338 by Virginia Tech, Wiley Online Library on [12/05/2023]. See the Terms and Conditions (https://onlinelibrary.wiley.com/remu

and-conditions) on Wiley Online Library for rules of use; OA articles are governed by the applicable Creat

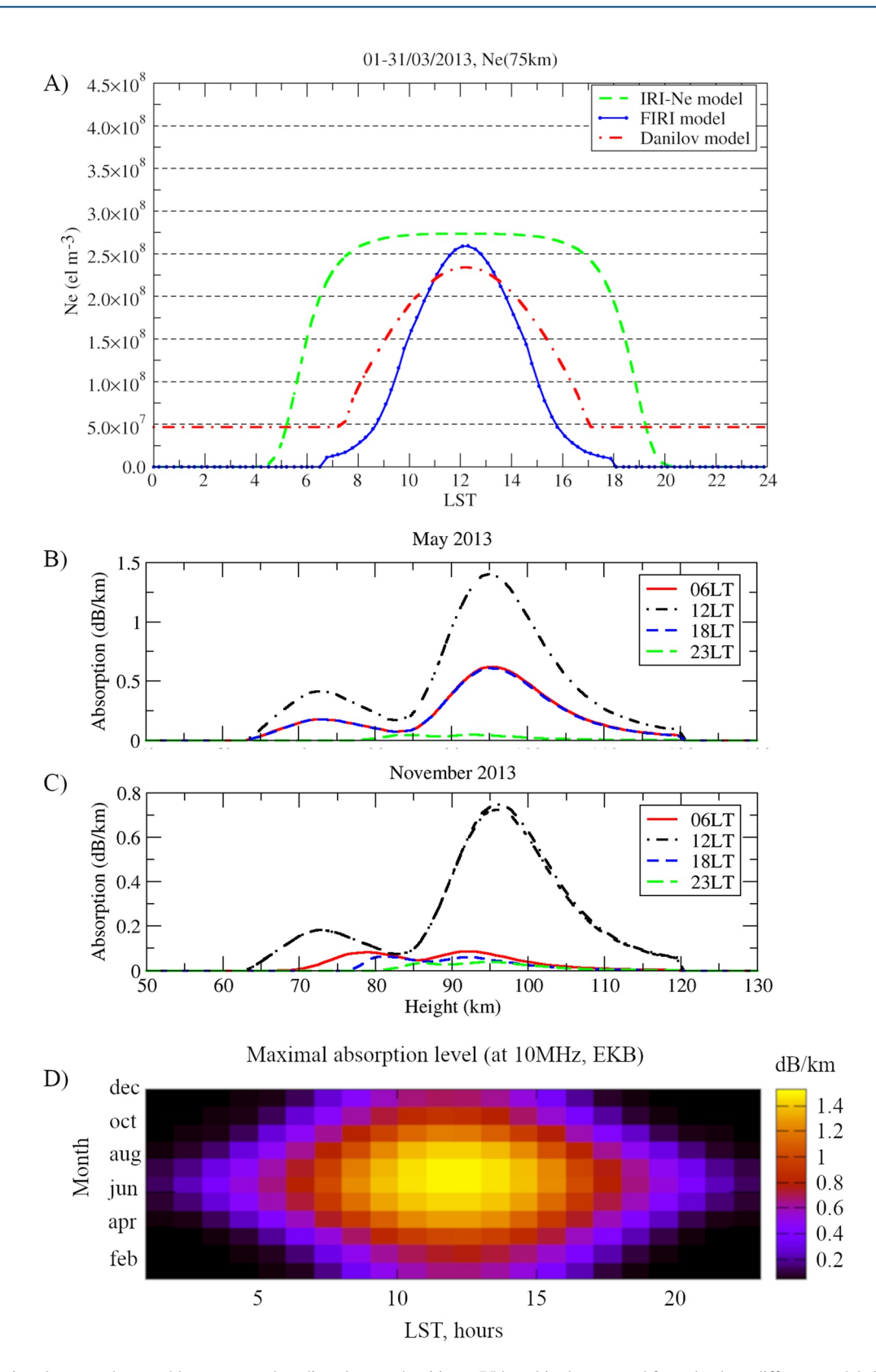


Figure 3. (a) Comparison between the monthly average and median electron densities at 75 km altitude extracted from the three different models listed in the legend. (b–d) Modeling results for beam 2 of the EKB radar (0° azimuth) for the year 2013, based on the standard IRI-Ne option of the model IRI-2012. (b) Modeled absorption profile per 1 km propagation trajectory for May 2013. Panel (c) same as panel (b), but for November 2013. (d) Seasonal-daily variation of the maximum value of the absorption per 1 km of the radio signal trajectory in the ionosphere.

BERNGARDT ET AL. 10 of 20

the standard IRI-2012 model to describe the D-layer. The radiowave propagation path used for the calculation corresponds to the trajectory of the groundscatter signal propagation, that is, to the trajectory from the skip zone boundary to the radar. The absorption values are close, in the end, to the results obtained by (Zawdie et al., 2017).

Figure 3d also shows the full seasonal-daily variation of the maximum value $L_{\text{max}}[dB]$ of absorption per km of the trajectory in the ionosphere

$$L_{\max}[dB] = Max \left(-L[dB]\right)_{h=[60..120\text{km}]} \tag{16}$$

The calculation is based on the standard IRI-2012 D-layer model for the EKB radar site. As can be seen, the maximum absorption is observed in the summer under daytime conditions. This is the result of the ionization of the lower part of the ionosphere being greatest at that time of day and year. It contrasts with winter and/or nighttime conditions when the lower ionosphere in non-disturbed regular conditions should have only weak ionization if any at all, according to the empirical models. Monitor measurements of these variations in non-regular conditions over the large area covered by radars field of views, is one of the tasks the suggested technique can be used for.

3. Results and Discussion

3.1. Comparison Between Simulations and Experimental Observations

For the years 2013 and 2014, we have compared the observed noise level for our four mid-latitude radars with calculations based on our noise level model using three different D-layer models included into the international reference ionospheric model IRI-2012: (a) the standard IRI-Ne (Bilitza, 1997) model, (b) the FIRI model (Friedrich & Torkar, 2001), and (c) the Danilov model (Danilov et al., 1995). For the comparison we used the following technique: using experimental data we determined the low cut-off levels, specific for each radar, to highlight seasonal-daily dynamics of the noise shown in (Berngardt, 2020; Ponomarenko et al., 2016) as they related with the solar terminator. By using this cut-off level, in fact, we cut the saturation effects in the low-intensity noise, as shown and discussed below in this paper. After choosing a cut-off level, we calculated the dynamic range of the resulting noise levels (from the maximal to the minimal values). We used it to determine the level of the model noise, after normalizing its maximum yearly value to 0 dB. As a result the dynamic range of the truncated model noise and truncated experimental noise became the same, allowing usto compare them. The comparisons are shown in Figure 4.

A detailed comparison can be made with more confidence for the data associated with the EKB and SAS radars, because the data from these radars came from noise level observations at a fixed frequency close to 10 MHz on a 24 hr per day basis. From the results displayed in Figures 4a–4d and 4i–4l for the EKB and SAS radars respectively, it can be seen that using the standard IRI-Ne D-layer model leads to a significant overestimation of noise absorption, while the FIRI and Danilov models offer a better qualitative agreement between model calculations and observations in regions away from the regions of low noise prediction by the model (i.e., the uniformly dark central areas in the panels that describe the computational results).

Data from the BKS and KER radars are harder to use for a comprehensive analysis because they come from a variety of daytime and nighttime sounding conditions. Nevertheless, the daytime data that were retrieved (for 14 MHz at BKS and for 10 MHz at KER) demonstrate a good agreement with our model, particularly for the KER radar and especially when using Danilov's model of the D-layer.

As one can see, the KER radar (southern hemisphere) seasonal-daily noise has a distribution that differs significantly from the northern hemisphere EKB, SAS, and BKS radars. This difference appears to come from the difference in hemispheres that are to be associated with different seasons and atmosphere/ionosphere conditions. Indeed our model shows a good correspondence with the observations in both the northern and southern hemispheres, implying that the model that we formulated based on Equation 2 has validity.

To make quantitative estimates, we used correlation analysis. As the analysis of both linear(Pearson) and range(Spearman) correlations has shown, the experiment correlates with Danilov's model of D-layer significantly better (0.55–0.70 for Pearson and 0.56–0.74 for Spearman) than with random values (0.09–0.47 and 0.11–0.54 correspondingly). We tested the correlation of the experimentally measured data with random values (uniformly distributed within cut level limits), and the correlation of the experimental data with model predictions. The significant increase

BERNGARDT ET AL. 11 of 20

1944/99x, 2022, 9. Downloaded from https://agupubs.onlinelibrary.wiley.com/doi/10.1029/2021RS007338 by Virginia Tech. Wiley Online Library on [12/05/2023]. See the Terms and Conditions (https://onlinelibrary.wiley.com/erms-and-conditions) on Wiley Online Library for rules of use; OA archies are governed by the applicable Creative Commons Licenses

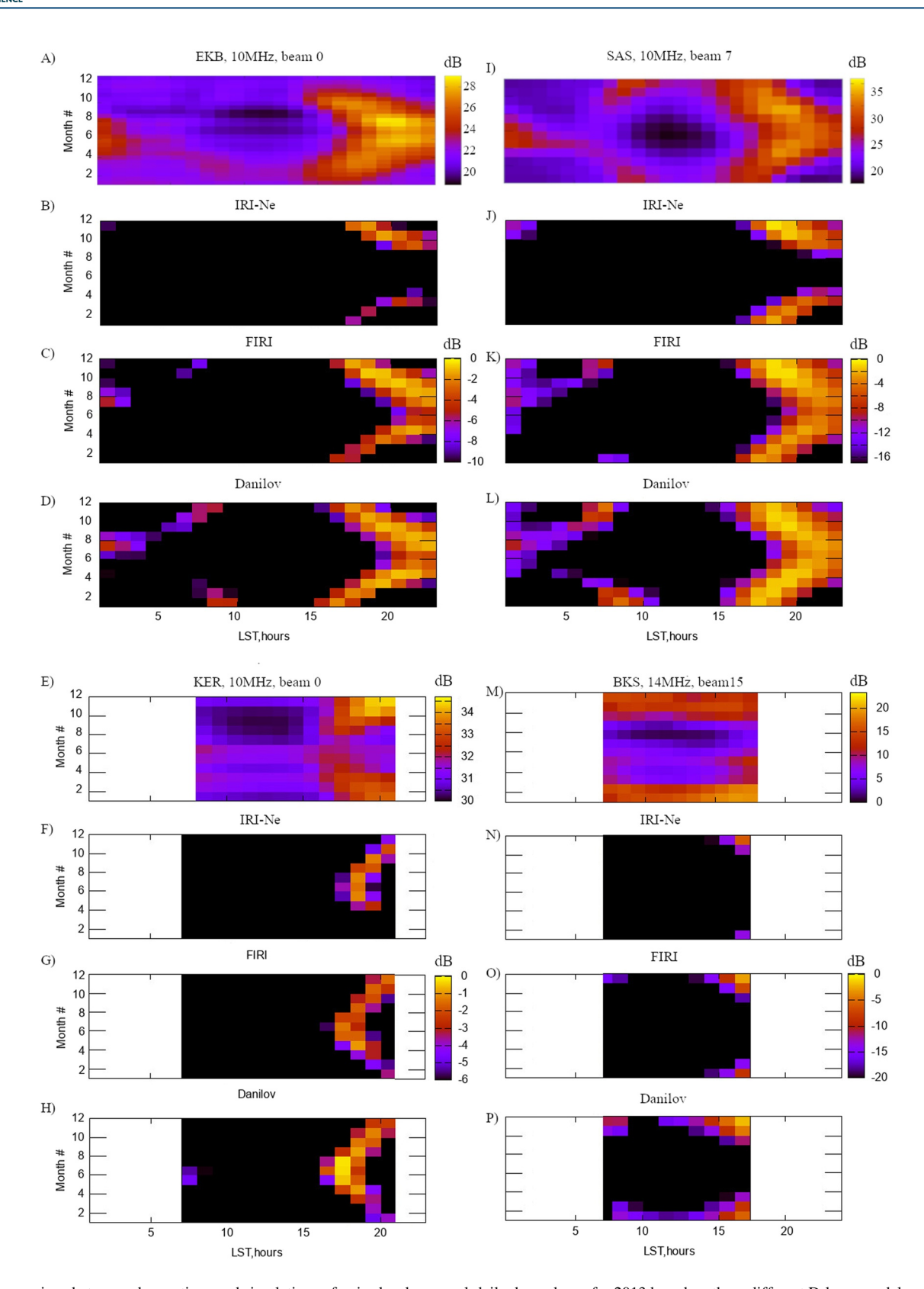


Figure 4. Comparison between observations and simulations of noise level seasonal-daily dependence for 2013 based on three different D-layer models, namely, IRI-2012, FIRI, and Danilov. Panels (a–d) show EKB radar, 10 MHz, at 0° azimuth with the top panel for observations and the next three panels for each model. Panels (e–h) same as panels (a–d), but for the KER radar at 10 MHz for a 180° azimuth. Panel (i) shows SAS observations reported by Ponomarenko et al. (2016). Panels (j–l) same as panels (b–d), but for the SAS radar at 10 MHz for a -23° azimuth. Panels (m–p) same as panels (a–d), but for the BKS radar at 14 MHz at 0° azimuth.

BERNGARDT ET AL. 12 of 20

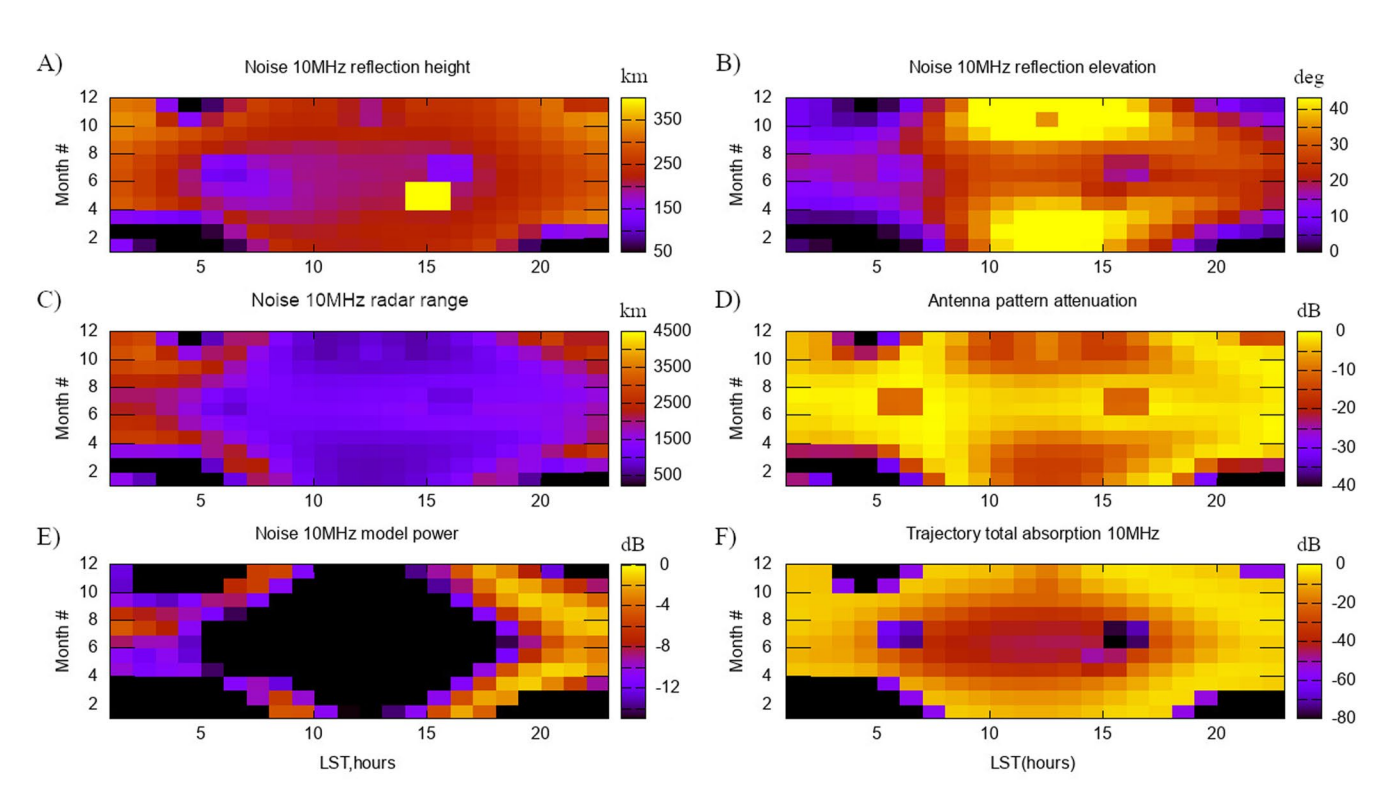


Figure 5. Simulated seasonal-diurnal variation of parameters associated with the propagation of radio waves for the EKB radar in 2013 at 10 MHz. We used the standard IRI-Ne model for the D-layer. (a) Noise reflection height; (b) noise reflection elevation angle; (c) radar range to most effective noise source (to skip-zone); (d) antenna pattern attenuation at calculated elevation angle; (e) resulting model noise level; and (f) total absorption over the calculated trajectory due to ionospheric absorption.

in correlation coefficients allows us to conclude that the model could be used to explain the seasonal-daily dynamics of the noise. The closely similar values of both the linear and range correlation coefficients allow us to expect a linear dependence between the model and experimental observations. The highest increase of the correlation (0.54–0.74 for model vs. 0.09–0.14 for random values) is observed at the EKB and SAS radars, with their 24 hr measurements of the noise at a fixed frequency. For the KER and BKS radars, providing only half-time measurements, this increase of the correlation coefficients is significantly weaker (0.60–0.71 for model vs. 0.26–0.54 for random values). RMSE of the model depends on the radar and form 0.9–6.6 dB. The table of results is given in Table S1.

3.2. Relationship Between Propagation Parameters and Noise Variations

For a qualitative analysis, it is useful to demonstrate the relationship between the propagation parameters and the seasonal-diurnal variation of the noise level. Figure 5 shows the simulated results of seasonal-diurnal variation of various propagation parameters at the EKB radar. It can be seen from the figure that:

- the annular shape of the noise level (Figure 5e) is controlled mainly by the total absorption over the propagation trajectory (Figure 5f): in other words, the more absorption there is, the less noise is seen, with the two patterns matching very well;
- the total absorption over the trajectory, in turn, is related to the trajectory elevation angle (which changes the propagation length of the signal in the absorbing layer)—the higher the elevation angle, the shorter this length and the higher the noise level (Figure 5b).
- the total absorption is also related to the unit absorption in the regular D- and E-layers—the stronger the absorption, the lower the noise level(Figure 5f vs. Figure 3d). We should note that preliminary modeling has shown that the absorption below 85 km altitude is comparable to the absorption above 85 km; and
- the attenuation of the noise level in the winter daytime is associated with antenna pattern attenuation at high elevation angles(Figure 5d vs. Figure 5b).

BERNGARDT ET AL. 13 of 20

Radio Science 10.1029/2021RS007338

3.3. Saturation Effect and Quiet Day Curve

As could be inferred from Figure 5, the central region embedding summer daytime conditions seems to be associated with noticeably weaker noise levels than expected from the model calculations. The predictions for weak noise levels are based on strong absorption during sunlit conditions so that little noise from ground sources should be expected to be found. We have carried out more detailed comparisons to assess this situation. For the purpose at hands, we focused on only two radars (EKB and SAS) because these were radars that used a fixed sounding frequency (10 MHz) on a continuous basis throughout the day. This allows for a numerical comparison between the model and observations: Figure 6 shows some detailed examples of daily variations of the noise on the EKB and SAS radars for different dates and their comparison with our proposed model when we use the Danilov D-layer model for taking into account absorption at lower altitudes, the IRI-2012 ionosphere model for taking into account propagation effects, and NRLMSISE-00 neutral atmosphere model for calculating the electron collision frequency.

As might have been expected from Figure 5, the various panels in Figure 6 show a satisfactory agreement between the observations and the model at high noise levels, but there is generally a strong disagreement when the model noise level is predicted to be low. We see two possibilities that could explain this situation. One is that there may well be a saturation effect associated with analog and digital sensitivity levels of the radars. Alternatively, or even in association with instrumental noise, cosmic noise could be a factor, as it can sometimes be as high as 20 dB below anthropogenic noise, as shown in Figures 2 and 39 of the ITU-R P.372-14 (2020) report. Cosmic noise comes from much higher elevation angles and could make a significant contribution when anthropogenic noise is not too strong because of absorption. Also tropical thunderstorm centers signals coming from backlobe could affect this saturation level. We have not queried this question any further as the focus of the present paper is anthropogenic sources from the ground. Our model of these contributions produces the bright arc patterns in Figure 4. The important message is that these arcs fit well with the notion of noise from anthropogenic sources.

To demonstrate that saturation effects are real, we introduce Figure 7. Figures 7a and 7b show the results of a statistical comparison between the model and the observations using the EKB and KER radar data in the year 2013. The color shows the number of cases when a particular combination of experimental and model noise values was obtained.

Consider Figure 7a first: clearly, when the observed noise level is less than 20 dB, there is no connection between the predicted noise level and the observed one. However, when the observed noise level is greater than 20 dB there is a linear relation between prediction and observations. From this it should be clear that the measured EKB noise levels are saturated below 20 dB, thereby having nothing to do with ionospheric absorption. By contrast, above 20 dB, the effects of ionospheric absorption are seen. The clear implication is that the model cannot be used below 20 dB in the EKB case because of noise saturation effects affecting the observations.

Figure 7b shows that a similar effect takes place for the KER radar. In that case, however, the saturation level is higher (32 or 33 dB), and the physical information that can be extracted from noise variations is for noise levels that are weaker by about 8–10 dB.

Figures 7c and 7d display similar information in a somewhat different way through monthly statistics. For those panels, we kept track of the radar data that could be suitably compared with a numerical interpretation of the observations by the proposed model (as per the numbers inferred from panels (a and c), meaning a noise level above 20 dB for the EKB radar and above 32 or 33 dB for the KER radar). This being the case, Figure 7c shows that the probability that the noise level at EKB be 20 dB above the numbers expected from our simulations is always above 60% at all times of the year, with a somewhat higher value (closer to 80%) in June. The numbers are different for KER, as seen from Figure 7d. We note that the statistics are too weak to give any significance to the June peak in that case (a change from 32 to 33 dB would put the peak well inside a region of minimum probability).

From our analysis of Figures 7a–7d we may conclude that about a half of the daily noise data at EKB is suitable for the numerical interpretation. These periods where the simulations work reasonably well are usually associated with a weak D-layer ionization level. They come mainly from nighttime and autumn-winter months. This much is clear after we take another look at Figure 4. The smaller size of the data set in KER is caused by its smaller

BERNGARDT ET AL. 14 of 20

1944/99x, 2022, 9. Downloaded from https://aguppubs.onlinelibrary.wiley.com/doi/10.1029/2021RS007338 by Virginia Tech, Wiley Online Library on [12/05/2023]. See the Terms and Conditions (https://onlinelibrary.wiley.com/rems-and-conditions) on Wiley Online Library for rules of use; OA articles are governed by the applicable Creared by the applicable Crear

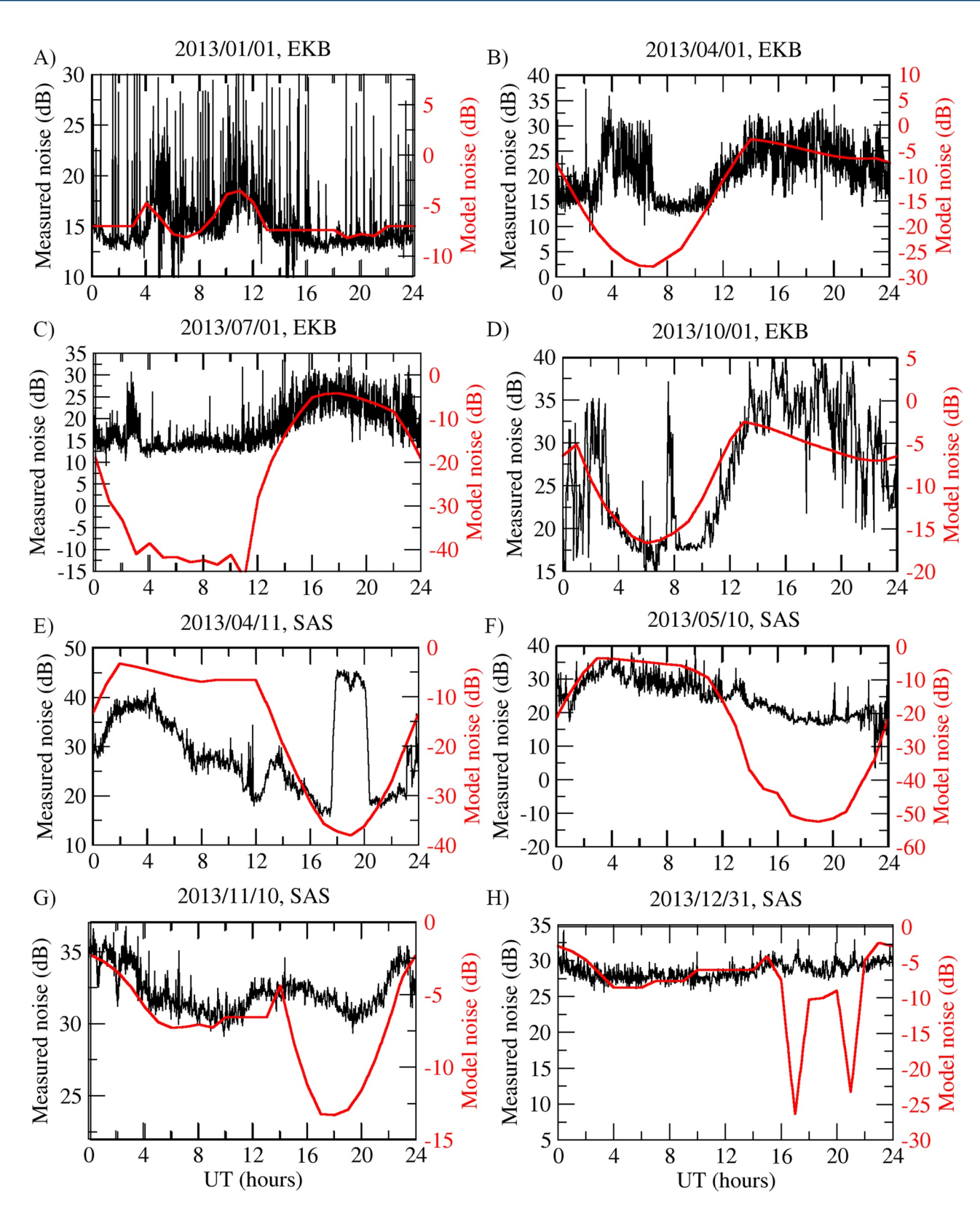


Figure 6. Comparison of model (red line) and measured daily noise variations (black line) on radars EKB (beam 2, (a-d)) and SAS (beam 7, (e-h)), at 10 MHz.

BERNGARDT ET AL. 15 of 20

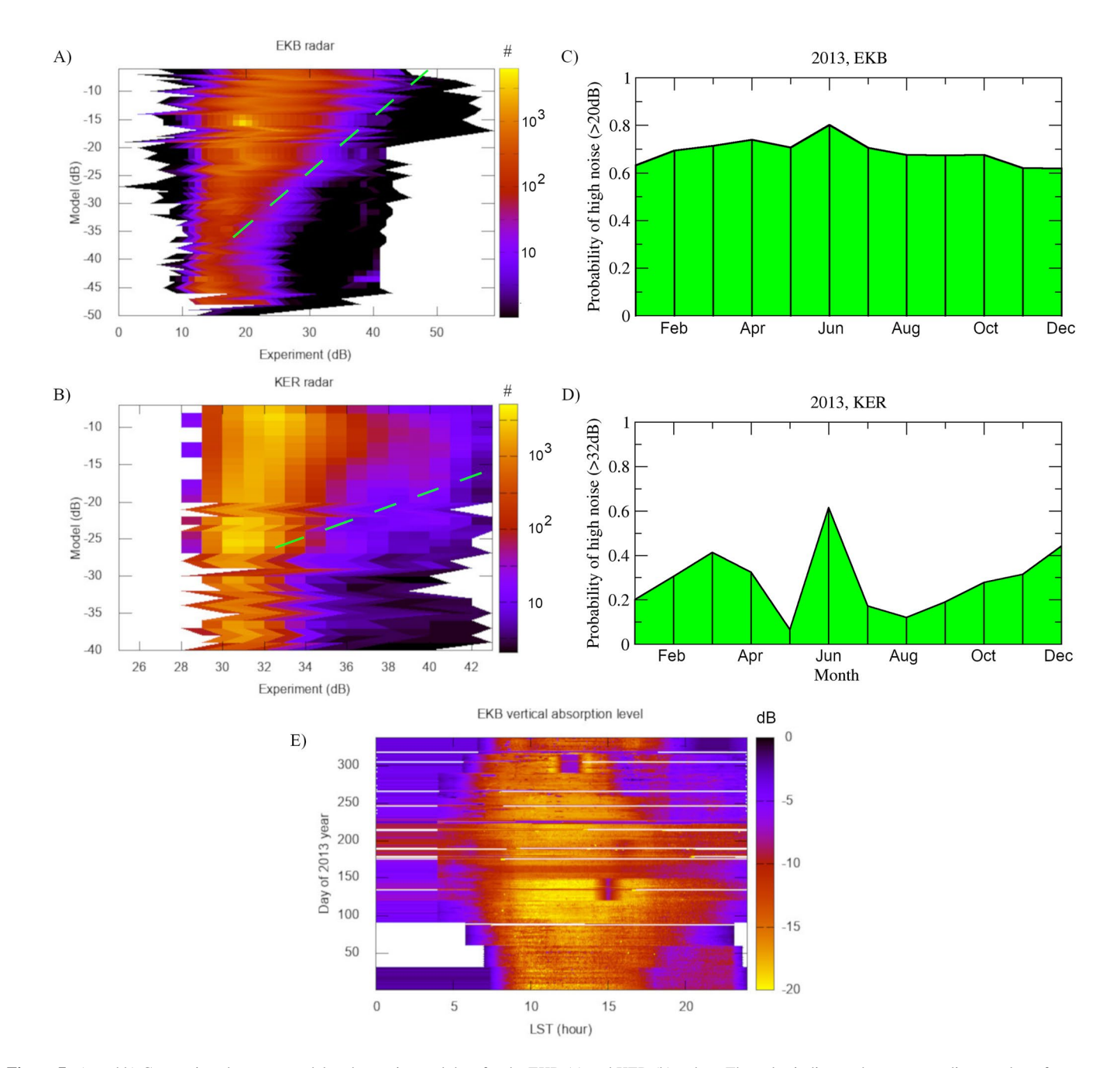


Figure 7. (a and b) Comparison between model and experimental data for the EKB (a) and KER (b) radars. The color indicates the corresponding number of occurences of combinations of experiment versus model values. Dashed line in panels (a and b) corresponds to linear dependence (i.e., exact prediction of experiment by the model). (c and d) Monthly statistics of radar data available for adequate numerical analysis within the framework of the proposed model: for EKB (c) and KER (d) radars. (e) Vertical absorption at 10 MHz calculated from experimental EKB noise data using the suggested model.

dynamical range (Figure 7b), itself most likely caused by a lower level of distributed surface anthropogenic sources around the radar (Figure 1c), which is isolated in the Southern Indian Ocean.

With the above reservations concerning extra noise sources in mind, the proposed model can be used to build a quiet day curve (the results of which are presented through the red traces in Figure 6). However, for the model to be put to good use, we need to take into account the saturation effect of the radar sensors at low noise levels. The saturation level clearly differs for each specific radar (Figures 7a and 7b), and its mechanism and dynamics should be studied in the future. The constant absolute difference(offset) between model and experiment is related to not

BERNGARDT ET AL. 16 of 20

om/doi/10.1029/2021RS007338 by Virginia Tech, Wiley Online Library on [12/05/2023]. See

taking into account a number of constant multipliers in the modeling. The lower experimental noise level than predicted by the model can be result of electron density increases unaccounted for by the ionospheric models. As shown above, this model depends on a number of factors, namely, (a) the trajectory of propagation of the noise signals (or ground-scatter signals), (b) the antenna pattern in the elevation plane of propagation, as well as (c) the mode of the received signal as it is affected by propagation in a three-dimensionally inhomogeneous ionosphere. The model used for the "quiet" ionospheric D-layer is also significant in the construction of the quiet day curve. The comparison of observations with model simulations (Figure 4) shows that the use of the traditional IRI-2012 model leads to significant overestimation of the noise level. The Danilov model of the D-layer leads to better fits to observed noise levels than the other models, at least for the EKB radar (Figure 4).

3.4. Implications for the Modeling of Ionospheric Absorption

Based on the use of Equation 2 for the construction of our model, one can exclude all propagation effects (antenna pattern attenuation G_A , radio wave attenuation with distance $\overline{A_R}$, and focusing effects $\overline{I_F}$) on the noise level variations $\overline{I_{N,rev}}$ as well as exclude attenuation variations in the elevation angles through propagation for a trajectory through an angle α in the D-layer (valid for a thin non-refracting absorption layer). In other words the intensity is essentially "fixed" through the relation

$$I_{N,fxd}[dB] = 10 \cdot \log_{10} \left(\frac{\overline{I_{N,rcv}}}{I_{0,N}\overline{I_F}G_A\overline{A_R}} \right)$$
(17)

while the vertical absorption becomes

$$A_{t,vert}[dB] = (I_{N,fxd}[dB] - Max(I_{N,fxd}[dB])) \cdot \sin(\alpha)$$
(18)

where the maximum value is calculated over the year to calibrate absorption when it reaches a minimum. As a result, one can obtain an estimate for the equivalent vertical absorption $A_{t,vert}$ near the radar. Figure 7e shows the seasonal-daily dynamics of the vertical absorption $A_{t,vert}$ near EKB based on this approach to the analysis of the noise observations at 10 MHz. As one can see, the vertical absorption goes through a maximum at summer daytime. This corresponds well, qualitatively, to the D-layer absorption expected from the IRI-2012 and NRLMSISE-00 models, as shown in Figure 3d.

3.5. Discussion on Model Accuracy

In this paper we used the IRI-2012 model. The model is admittedly rather old, and improvements have been made in IRI-2016 (Bilitza et al., 2017) while some new models of the high-latitude ionosphere have been developed (Shubin, 2017; Themens, Jayachandran, McCaffrey, Reid, et al., 2019; Themens et al., 2017). Our study has shown the basic path to the modeling of the minimal noise. The impact of newer models will be tested in the future through their inclusion in our simulations. It should also be kept in mind that each model can only approximate reality, so that calibration with ionosondes or SuperDARN groundscatter data would have to be taken into consideration in future modeling efforts so as to provide better and more accurate ray-tracing. Using only ionospheric models could cause up to tens of percent uncertainties in the electron density (Bjoland et al., 2016; Liu et al., 2019; Themens, Jayachandran, & McCaffrey, 2019). In ray-tracing parameters, such as elevation angle, the error/uncertainty could have even greater impact since, particularly at night, the electron density could be so low that focusing could not take place at all, meaning no ground scatter signals in the radar data.

The contribution to absorption due to magnetic field effects on the ray paths can be estimated by using the fact that the magnetic field correction to absorption involves the factor $(1 + \epsilon)$ where

$$\epsilon = 2w_{ecf} * \cos(\theta) / (2\pi f_0), \tag{19}$$

where w_{ecf} is the electron cyclotron frequency, and θ is the angle between the radiowave trajectory and the magnetic field. This expression for the magnetic field correction can easily be derived, for example, from Equation 2 in the paper by Zawdie et al. (2017). It can be shown from this that not taking into account the magnetic field in oblique propagation at mid- and high-latitudes ($\theta \approx 90^{\circ}$) has a less than 15% effect, which is less than errors caused by the ionospheric model. This justifies not taking into account the magnetic field. The same reasoning is used to justify

BERNGARDT ET AL. 17 of 20

not taking the magnetic field into account in the ray-tracing algorithms (Equations 4 and 5). That is to say, in the first approximation we can neglect magnetic field effects as long as $w_{ecf} \ll 2\pi f_0$, as Ginzburg (1970) had indicated in the past. This assumption holds true to first order for the frequencies used in our work.

The assumption of homogeneous and stationary noise sources in Equation 2 also could be a source of errors. For example, it clearly cannot be justified near thunderstorm activity centers in equatorward-oriented radars (Pederick & Cervera, 2014, 2016).

Finally, when calculating focusing effects to first order (Equation 6), we expect that spatial gradients over latitude and longitude are small. This is correct for IRI, but could be incorrect in the actual ionosphere. In the presence of strong gradients and medium-size irregularities the model could be modified following the prescription posted by Afanasiev et al. (1998), but this would need a much more accurate ionospheric model than what we have used at this point.

4. Conclusion

In this paper, we have developed a numerical model of the seasonal-diurnal dynamics of the radio noise at polar-oriented HF-radars. The model has focused on four HF mid-latitude coherent scatter radars—EKB from ISTP SB RAS, and SAS, BKS and KER from SuperDARN. The numerical results have been compared with observations.

The results from our simulations give credence to the model proposed earlier in Berngardt et al. (2018, 2019) for interpreting the radio noise level in terms of the spatial focusing of ground sources of anthropogenic origin in the vicinity of the "skip zone" propagation boundary. Using the IRI-2012 and NRLMSISE-00 models, it has been shown here that seasonal-diurnal variations of the noise level can be explained within the framework of this model through a combination of propagation, absorption and antenna pattern factors.

We have demonstrated that the seasonal-diurnal patterns observed in radio noise (with a maximum in the region of the solar terminator) is associated with variations in the total absorption of the signal over the propagation trajectory to the border of the skip zone. We have also shown that an observed decrease in the noise intensity in the winter noon area in the EKB and SAS radars (not detected with the BKS radar) can be explained by an additional attenuation of the signal by the antenna beam pattern at high elevation angles.

The agreement with observations is particularly good near the terminator where the noise level is greatest. This has allowed to us compare the absorption computed from different D region models and compare the resulting noise levels with observations. We found that the absorption levels, when integrated along the ray paths, were too high when using the standard IRI-2012 D-layer model. However, the agreement with observations based on the use of the FIRI (Friedrich & Torkar, 2001) and Danilov (Danilov et al., 1995) D-layer models was much better.

The above notwithstanding, in spite of a good qualitative agreement of the seasonal-diurnal model variations with observations, quantitative simulation results demonstrate that the model predicts far less noise than observed away from the terminator during sunlit conditions. There are only two possible explanations: either the model produces too much absorption, or there is another source of noise that does not involve ground-based anthropogenic sources. In the former case, one would have to face the fact that the model produces realistic amounts of absorption at other times, particularly near the terminators. In the latter case there are two possibilities, both of which must be present but were not considered for our model based on ground sources: cosmic background noise, which comes from above and would favor larger elevation angles, and instrumental noise, that is, saturated noise counts. The ability to measure absorption variations from radar noise measurements depends on the surrounding anthropogenic noise level—the higher the noise level, the stronger absorption events the radar can study. For radars with low anthropogenic noise level, such as KER, it may be difficult to study strong vertical absorption events from the noise data.

The main message to carry from the present study is that (a) the mechanism proposed in (Berngardt et al., 2018, 2019) does very well near the terminator where the noise level is at its strongest. Also, (b) there are additional noise sources to worry about, be they instrumental or of cosmic origin. Finally, (c) the present model should provide a useful tool for the assessment of absorption on a day-to-day basis. This means that we could

BERNGARDT ET AL. 18 of 20

1944799x, 2022, 9, Downloaded

om/doi/10.1029/2021RS007338 by Virginia Tech, Wiley Online Library on [12/05/2023]. See

Acknowledgments

The work of EKB radar was financially

supported by the Ministry of Science

Federation. Work of O. I. Berngardt

NCNI_a. J.-P. St.Maurice receives

and A. Marchaudon was supported by

joint RFBR-CNRS grant #21-55-15012

support from the Canadian NSERC. The

authors acknowledge the use of SuperD-

ARN data. SuperDARN is a collection

of radars funded by national scientific

funding agencies of Australia, Canada,

South Africa, United Kingdom, and the

USA. The authors thank all participants in

the worldwide SuperDARN collaboration

for the distribution of SuperDARN data

php?page=Data+Access. The Saskatoon

SuperDARN radar operations are specif-

Agency contracts and by a Major Science

Initiative from the Canada Foundation for

Toulouse University, and CNES) and was

funded by the IPEV and CNRS through

INSU and PNST programs. The Super-

DARN Blackstone radar is operated by

the Virginia Tech with funding from the

AGS-1935110

National Science Foundation under award

via http://vt.superdarn.org/tiki-index.

ically funded by the Canadian Space

Innovation. The SuperDARN Kergue-

len radar is operated by IRAP (CNRS,

China, France, Italy, Japan, Norway,

and Higher Education of Russian

use the present numerical model or its successors to extract important information from the dynamics of noise measured by pole-oriented coherent scatter radars in the 8–20 MHz range.

It should be kept in mind that the results presented here can only be considered as preliminary, as they use reference ionospheric model IRI-2012 to calculate the propagation trajectory. For more correct calculations of the propagation path one really ought to take into account actual ionospheric refraction, estimated either from radar data (using, e.g., ground-scatter signals in combination with measured elevation angles) or from ionospheric electron density measurements by ionosondes. This approach will be considered in future studies.

Data Availability Statement

The data of EKB radar were obtained using the equipment of Center for Common Use "Angara" http://ckp-rf.ru/ckp/3056/ and available at http://sdrus.iszf.irk.ru/ekb/page_example/simple.

References

- Afanasiev, N. T., Zheonykh, A. A., Sazhin, V. I., Tinin, M. V., & Ivelskaya, M. K. (1998). Effects of large-scale clouds of ionospheric irregularities on the propagation of high-frequency radiowaves. *Journal of Atmospheric and Solar-Terrestrial Physics*, 60(17), 1687–1694. https://doi.org/10.1016/S1364-6826(98)00087-X
- Arnold, N. F., Cook, P. A., Robinson, T. R., Lester, M., Chapman, P. J., & Mitchell, N. (2003). Comparison of D-region Doppler drift winds measured by the SuperDARN Finland HF radar over an annual cycle using the Kiruna VHF meteor radar. *Annales Geophysicae*, 21(10), 2073–2082. https://doi.org/10.5194/angeo-21-2073-2003
- Berngardt, O. I. (2020). Noise level forecasts at 8-20 MHz and their use for morphological studies of ionospheric absorption variations at EKB ISTP SB RAS radar. Advances in Space Research, 66(2), 278–291. https://doi.org/10.1016/j.asr.2020.04.005
- Berngardt, O. I., Fedorov, R. R., Ponomarenko, P., & Grkovich, K. V. (2020). Interferometric calibration and the first elevation observations at EKB ISTP SB RAS radar at 10–12 MHz. *Polar Science*, 28, 100628. https://doi.org/10.1016/j.polar.2020.100628
- Berngardt, O. I., Ruohoniemi, J. M., Nishitani, N., Shepherd, S. G., Bristow, W. A., & Miller, E. S. (2018). Attenuation of decameter wavelength sky noise during x-ray solar flares in 2013–2017 based on the observations of midlatitude HF radars. *Journal of Atmospheric and Solar-Terrestrial Physics*, 173, 1–13. https://doi.org/10.1016/j.jastp.2018.03.022
- Berngardt, O. I., Ruohoniemi, J. M., St-Maurice, J.-P., Marchaudon, A., Kosch, M. J., Yukimatu, A. S., et al. (2019). Global diagnostics of ionospheric absorption during X-ray solar flares based on 8- to 20-MHz noise measured by over-the-horizon radars. *Space Weather*, 17(6), 907–924. https://doi.org/10.1029/2018SW002130
- Bilitza, D. (1981). Electron density in the D-region as given by the IRI, In International Reference Ionosphere IRI 79. In V. Lincoln, R. Conkright, &, K. Rawer (Eds), Rep. UAG-, pp. 7-10, World Data Center. A for Solar Terrestrial Physics
- Bilitza, D. (1997). International reference ionosphere Status 1995/96. Advances in Space Research, 20(9), 1751–1754. https://doi.org/10.1016/ S0273-1177(97)00584-X
- Bilitza, D., Altadill, D., Truhlik, V., Shubin, V., Galkin, I., Reinisch, B., & Huang, X. (2017). International Reference Ionosphere 2016: From ionospheric climate to real-time weather predictions. *Space Weather*, 15(2), 418–429. https://doi.org/10.1002/2016SW001593
- Bilitza, D., Altadill, D., Zhang, Y., Mertens, C., Truhlik, V., Richards, P., et al. (2014). The international reference ionosphere 2012 A model of international collaboration. *Journal of Space Weather and Space Climate*, 4, A07. https://doi.org/10.1051/swsc/2014004
- Bilitza, D., & Reinisch, B. (2008). International reference ionosphere 2007: Improvements and new parameters. *Advances in Space Research*, 42(4), 599–609. https://doi.org/10.1016/j.asr.2007.07.048
- Bjoland, L. M., Belyey, V., Løvhaug, U. P., & La Hoz, C. (2016). An evaluation of International Reference Ionosphere electron density in the polar cap and cusp using EISCAT Svalbard radar measurements. *Annales Geophysicae*, 34(9), 751–758. https://doi.org/10.5194/angeo-34-751-2016 Bland, E. C., Heino, E., Kosch, M. J., & Partamies, N. (2018). SuperDARN radar-derived HF radio attenuation during the September 2017 solar
- proton events. Space Weather, 16(10), 1455–1469. https://doi.org/10.1029/2018sw001916

 Bland, E. C., Partamies, N., Heino, E., Yukimatu, A. S., & Miyaoka, H. (2019). Energetic electron precipitation occurrence rates determined using the Syowa East SuperDARN radar. Journal of Geophysical Research: Space Physics, 124(7), 6253–6265. https://doi.org/10.1029/2018JA026437
- Danilov, A., Rodevich, A., & Smirnova, N. (1995). Problems with incorporating a new D-region model into the IRI. *Advances in Space Research*, 15(2), 165–168. (Off Median Phenomena and International Reference Ionosphere). https://doi.org/10.1016/S0273-1177(99)80042-8
- Danilov, A., Smirnova, N., Blix, T., & Thrane, E. (2002). A new concept of the D-region modeling at high latitudes. *Advances in Space Research*, 29(6), 919–927. https://doi.org/10.1016/S0273-1177(02)00048-0
- 29(6), 919–927. https://doi.org/10.1016/S02/3-117/(02)00048-0
 Friedrich, M., & Torkar, K. M. (2001). Firi: A semiempirical model of the lower ionosphere. *Journal of Geophysical Research*, 106(A10),
- 21409–21418. https://doi.org/10.1029/2001JA900070
 Ginzburg, V. (1970). The propagation of electromagnetic waves in plasmas. Pergamon Press.
- Gomonov, A. D., Yurik, R. Y., Shapovalova, Y. A., Cherniakov, S. M., & Kalitenkov, N. V. (2019). The analysis of electron density values according to simulations by IRI Model and from experimental measurements by partial reflection radar. In 2019 Russian Open Conference on Radio Wave Propagation (RWP). IEEE, https://doi.org/10.1109/rwp.2019.8810341
- ITU-R P.372-14. (2020). Recommendation ITU-R P.372-14 (08/2019). Radio noise. Retrieved from https://www.itu.int/rec/R-REC-P.372-14-201908-I/en
- Kravtsov, Y. (1968). On two new asymptotic methods in the theory of wave propagation in inhomogeneous media. Overview (in Russian). Acoustical Journal, 14(1), 1–24.
- Kravtsov, Y., & Orlov, Y. (1983). Caustics, catastrophes, and wave fields. Soviet Physics Uspekhi, 26(12), 1038–1058. https://doi.org/10.1070/pu1983v026n12abeh004582
- Liu, Z., Fang, H., Weng, L., Wang, S., Niu, J., & Meng, X. (2019). A comparison of ionosonde measured foF2 and IRI-2016 predictions over China. Advances in Space Research, 63(6), 1926–1936. https://doi.org/10.1016/j.asr.2019.01.017
- Pederick, L. H., & Cervera, M. A. (2014). Semiempirical model for ionospheric absorption based on the NRLMSISE-00 atmospheric model. Radio Science, 49(2), 81–93. https://doi.org/10.1002/2013RS005274

BERNGARDT ET AL. 19 of 20

1944799x, 2022, 9, Downloaded

com/doi/10.1029/2021RS007338 by Virginia Tech, Wiley Online Library on [12/05/2023]. See the Terms and Conditions (https://onlinelibrary.wiley.com/rerm:

and-conditions) on Wiley Online Library for rules of use; OA articles

are governed by the applicable Creativ

- Pederick, L. H., & Cervera, M. A. (2016). A directional HF noise model: Calibration and validation in the Australian region. *Radio Science*, 51(1), 25–39. https://doi.org/10.1002/2015rs005842
- Ponomarenko, P., Iserhienrhien, B., & St-Maurice, J.-P. (2016). Morphology and possible origins of near-range oblique HF backscatter at high and midlatitudes. *Radio Science*, 51(6), 718–730. https://doi.org/10.1002/2016rs006088
- Samson, J. C., Greenwald, R. A., Ruohoniemi, J. M., Frey, A., & Baker, K. B. (1990). Goose Bay radar observations of Earth-reflected, atmospheric gravity waves in the high-latitude ionosphere. *Journal of Geophysical Research*, 95(A6), 7693–7709. https://doi.org/10.1029/ JA095iA06p07693
- Schunk, R. W., & Nagy, A. F. (2000). Ionospheres: Physics, plasma physics, and chemistry. Cambridge University Press. https://doi.org/10.1017/CBO9780511551772
- Shepherd, S. G. (2014). Altitude-adjusted corrected geomagnetic coordinates: Definition and functional approximations. *Journal of Geophysical Research: Space Physics*, 119(9), 7501–7521. https://doi.org/10.1002/2014JA020264
- Shepherd, S. G. (2017). Elevation angle determination for SuperDARN HF radar layouts. Radio Science, 52(8), 938–950. https://doi.org/10.1002/2017RS006348
- Shubin, V. N. (2017). Global empirical model of critical frequency of the ionospheric F2-layer for quiet geomagnetic conditions. *Geomagnetism and Aeronomy*, 57(4), 414–425. https://doi.org/10.1134/s0016793217040181
- and Aeronomy, 57(4), 414–425. https://doi.org/10.1134/s0016793217040181

 Sterne, K. T., Greenwald, R. A., Baker, J. B. H., & Ruohoniemi, J. M. (2011). Modeling of a twin terminated folded dipole antenna for the Super
- Dual Auroral Radar Network (SuperDARN). In 2011 IEEE RadarCon (RADAR) (pp. 934–938). https://doi.org/10.1109/RADAR.2011.5960673
 Themens, D. R., Jayachandran, P., McCaffrey, A. M., Reid, B., & Varney, R. H. (2019). A Bottomside parameterization for the empirical Canadian high arctic ionospheric model. Radio Science, 54(5), 397–414. https://doi.org/10.1029/2018rs006748
- Themens, D. R., Jayachandran, P. T., Galkin, I., & Hall, C. (2017). The empirical Canadian high arctic ionospheric model (E-CHAIM): N_mF₂ and h_mF₃. *Journal of Geophysical Research: Space Physics*, 122(8), 9015–9031. https://doi.org/10.1002/2017ja024398
- Themens, D. R., Jayachandran, P. T., & McCaffrey, A. M. (2019). Validating the performance of the Empirical Canadian High Arctic Ionospheric Model (e-CHAIM) with in situ observations from DMSP and CHAMP. *Journal of Space Weather and Space Climate*, 9, A21. https://doi.org/10.1051/swsc/2019021
- Themens, D. R., Jayachandran, P. T., Nicolls, M. J., & MacDougall, J. W. (2014). A top to bottom evaluation of IRI 2007 within the polar cap. Journal of Geophysical Research: Space Physics, 119(8), 6689–6703. https://doi.org/10.1002/2014ja020052
- Tinin, M. V., Afanasyev, N. T., Mikheev, S. M., Pobedina, A. P., & Fridman, O. V. (1992). On some problems of the theory of radio wave propagation in a randomly inhomogeneous ionosphere. *Radio Science*, 27(2), 245–255. https://doi.org/10.1029/91RS02921
- Zawdie, K. A., Drob, D. P., Siskind, D. E., & Coker, C. (2017). Calculating the absorption of HF radio waves in the ionosphere. *Radio Science*, 52(6), 767–783. https://doi.org/10.1002/2017RS006256

BERNGARDT ET AL. 20 of 20